Chemical Engineering Journal 396 (2020) 125273

Contents lists available at ScienceDirect

Chemical Engineering Journal

journal homepage: www.elsevier.com/locate/cej

Analysis of equilibrium and dynamic adsorption of benzene vapor over unimodal and bimodal silica-based mixed-metal oxides

Busuyi O. Adebayo, Shane Lawson, Ali A. Rownaghi, Fateme Rezaei*,[1]

Department of Chemical & Biochemical Engineering, Missouri University of Science and Technology, 1101 N State Street, Rolla, MO 65409, United States

HIGHLIGHTS

- Synthesis of unimodal and bimodal silica-based mixed-metal oxide adsorbents.
- Higher equilibrium benzene vapor uptake for unimodal adsorbents than bimodal materials.
- Faster adsorption kinetics for bimodal adsorbents relative to unimodal materials.
- Titania-doped adsorbents showed higher adsorption capacities over zirconia-doped analogous.

GRAPHICAL ABSTRACT

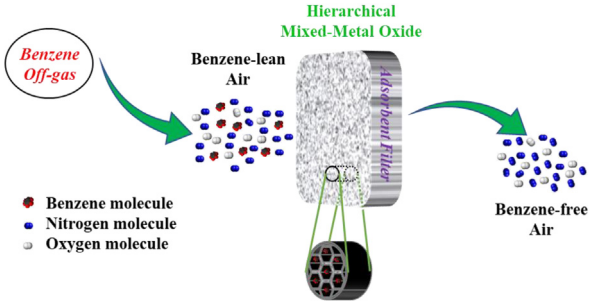

ARTICLE INFO

Keywords:
Benzene vapor
Adsorption
Mixed-metal oxide
Unimodal silica
Bimodal silica

ABSTRACT

In this study, purification of a benzene-lean gas stream over unimodal and bimodal silica-based mixed-metal oxides was investigated for the purpose of understanding the effects of secondary metal oxide and support pore structure on the adsorption capacities and kinetics. The unimodal silica fell in the borderline of micropores and mesopores, i.e., they consisted of large micropores and small mesopores with large surface area, while the bimodal silica consisted of large micropores, small mesopores and large mesopores with large mesopore volume. The titania and zirconia mixed-metal oxides showed reduced surface area and pore volume as a result of partial blockage of the pores, however, they exhibited improved adsorption behavior relative to the bare silica. Equilibrium adsorption measurements revealed unimodal adsorbents are superior to their bimodal analogues by exhibiting higher benzene vapor uptake, with capacities reaching 10.05, 11.71 and 11.25 mmol/g for SiO_2, TiO_2/SiO_2 and ZrO_2/SiO_2 samples at 25 °C and 101 kPa. In contrast, dynamic breakthrough tests with 465 ppm benzene vapor concentration indicated faster adsorption kinetics for bimodal adsorbents relative to unimodal materials as a result of their larger pores which produced lesser intraparticle diffusion resistance. It was also found that, while titania or zirconia incorporation enhances the equilibrium adsorption capacity of the bare silica, it deteriorates the adsorption rate. Similarly, all the adsorbents depicted partition coefficient in the range of 0.31–1.75 mmol/g/μM. The mass transfer coefficients estimated from concentration profiles of bimodal SiO_2, TiO_2/SiO_2 and ZrO_2/SiO_2 samples were 0.58 and 0.45, and 0.41 s^{-1}, respectively. Overall, the findings of this investigation indicated that the introduction of large mesopores in the structure of microporous-mesoporous silica is a facile approach in developing mixed-metal oxide adsorbents with improved adsorption capacity and kinetics for the abatement of benzene vapor emissions.

* Corresponding author.
E-mail address: rezaeif@mst.edu (F. Rezaei).
[1] ORCID: 0000-0002-4214-4235.

https://doi.org/10.1016/j.cej.2020.125273
Received 22 February 2020; Received in revised form 27 April 2020; Accepted 28 April 2020
Available online 30 April 2020

1. Introduction

Among various types of volatile organic compounds (VOCs), aromatic hydrocarbons, in particular benzene, toluene, xylene (BTX) compounds, are extremely harmful to human health and environment. BTX compounds are known carcinogens and their high concentration is linked to urban photochemical smog and ozone depletion [1,2]. While stringent environmental regulations imposed by governments have resulted in significant reductions in BTX emissions, their high concentrations in waste process streams are still a concern [3]. To address this, several biological, chemical and physical methods have been developed to capture and/or destroy these compounds [4,5]. Although these methods can capture and sequester sizable amounts of BTX, they suffer from some drawbacks including deficiency in treating low-concentration feeds, production of harmful byproducts, and high operation costs, which make them unattractive for scale-up [6].

To address these drawbacks, alternative methods have been developed in recent years for VOCs' emission control, among which adsorption appears to be an attractive approach especially for treating ultralow-concentration feeds because it allows for passive acquisition of BTX compounds without the production of toxic byproducts. In that regard, development of efficient and cost-effective adsorbents and processes has become a necessary area of research for BTX removal. To date, several classes of porous materials have been evaluated as BTX adsorbents including activated carbons, zeolites, metal–organic frameworks (MOFs), and metal oxides [7–9]. Carbon based materials possess some limitations, particularly risk of ignition during thermal regeneration by hot air and reduced VOC adsorptive capacity when relative humidity exceeds 70% [10]. Competitive adsorption of water over zeolites compromises the uptake capacity, thus serving as a hindrance toward their utilization at industrial scale. Moreover, although several MOFs such as MIL-101 and HKUST-1 have shown superior adsorption capacities for aromatic VOCs at low concentrations, their chemical and structural stability in humid atmosphere is a major concern for their utilization in this application [3,11,12].

On the other hand, metal oxides such as silica, alumina, titania, and zirconia with polar surfaces have been shown to effectively remove a wide variety of VOCs [13,14]. However, single metal oxides have their own limitations, such as high degree of hydrophilicity (e.g., in the case of silica), which leads to co-adsorption of water under normal conditions, reduced surface area and pore volume (e.g., in the case of titania or zirconia) and in general lower adsorption capacities [15–18]. To overcome these drawbacks, single metal oxides are often doped with heteroatoms via grafting, impregnation, or co-synthesis to form mixed metal oxides (MMOs) such as TiO_2/SiO_2, ZrO_2/SiO_2, TiO_2/ZrO_2 and ZrO_2/TiO_2 [19,20]. For instance, Ook Seo et al. [21] reported a 50% increase in toluene dynamic adsorption capacity for TiO_2/SiO_2 over the bare silica under dry conditions. In a study by our group [22], we synthesized several TiO_2/SiO_2 and ZrO_2/SiO_2 MMOs with varied metal loadings using a unimodal mesoporous UVM-7 SiO_2 and applied them for formaldehyde adsorption. The materials exhibited good surface characteristics, along with high formaldehyde uptake at optimum metal loadings, due to their high hydroxyl group content. Although incorporating heteroatoms that usually have higher affinity toward VOC compounds is a facile way of enhancing adsorption capacity [19], in many cases adsorption kinetics are compromised due to partial blockage of the support micropores which reduces the rate of mass transfer. In a study conducted by Liotta et al. [3] supported noble metals were used for hybrid adsorption catalysis of VOCs. They reported higher performance due to synergetic effect of the doped heteroatoms.

One way to address this issue and improve the mass transfer characteristics of MMOs is to use hierarchically structured supports that contain both micro- and mesopores. These solids can provide many characteristics missing in non-porous and even unimodal porous materials, such as better accessibility to active adsorption sites or higher activity in the oxidation of VOCs. For instance, in a study conducted by Wang et al. [23], hierarchical HZSM-5 zeolite doped with Ru was shown to be an efficient adsorbent/catalyst for abatement of bulky aromatic VOCs, because of its increased external surface and mesoporous volume, which resulted in shortened diffusion length by reducing intraparticle diffusional resistance. Recent studies have demonstrated the feasibility of preparing hierarchical metal oxides with macro- and mesoporosity and improved adsorption or catalytic activity compared to their microporous nanoparticle analogues [24–26].

Aiming at developing novel adsorbents with high capacity and enhanced kinetics, we embarked on a study to incorporate titania and zirconia into a bimodal microporous-mesoporous silica with two sizes of mesopores for abatement of benzene vapor as the model component of BTX. For comparison, we also synthesized a unimodal microporous-mesoporous silica with one size mesopores and doped the same amounts of titania and zirconia to demonstrate the advantages of bimodal silica in adsorbing benzene vapor with high capacity and fast kinetics. Adsorption behaviors were compared based on equilibrium and dynamic adsorption measurements. Finally, breakthrough profiles were fitted to estimate the mass transfer parameters in order to investigate the kinetics of benzene-lean air purification in detail.

2. Experimental section

2.1. Materials

All the chemicals used in this work including tetraethyl orthosilicate (TEOS, 99%), zirconium (IV) propoxide (ZrP, 70% in 1-propanol), titanium (IV) butoxide (TiB, 97%), triethanol-amine (TEAH, 98%), nitric acid (HNO_3, 70%), hexadecyltrimethylammonium bromide (CTAB), and polyethylene glycols (PEG) were all purchased from Sigma-Aldrich. Ammonium hydroxide (NH_3OH, 28.4%) was purchased from Fisher-Scientific. These chemicals were used as purchased without further purification. Ultrahigh purity nitrogen and helium gases were purchased from Airgas.

2.2. Adsorbent synthesis

2.2.1. Unimodal Silica-based adsorbents

These materials were prepared according to a modified synthesis route described by Ortiz De Zarate et al. [27]. Briefly, for each of the adsorbents, about 18 g of TEOS was added dropwise to 18 mL of TEAH at 25 °C, followed by the addition of required amount of metal alkoxide (ZrP or TiB). Using a ramp rate of 5 °C/min, the solution was heated to 150 °C and held at this temperature for 30 min to obtain atrane complexes, and subsequently cooled to 90 °C followed by the addition of CTAB. Thereafter, the resulting solution was cooled to 60 °C, allowed to get stabilized at that temperature for 5 min, and mixed with 150 mL of DI water. Up to this point, the synthesis was carried out in an oil bath under magnetic stirring at 350 rpm. The obtained solution was then left to gel without agitation for 24 h at room temperature, after which it was washed 3 times with DI water for 5 h then 3 times with ethanol for 5 h before drying for 2 days at room temperature. The synthesized unimodal bare SiO_2 was named S1, whereas the unimodal TiO_2/SiO_2 and ZrO_2/SiO_2 were denoted as S2 and S3, respectively.

2.2.2. Bimodal silica-based adsorbents

These materials were prepared by following the synthesis route described by Smått et al. [24]. Firstly, for each of the adsorbents, an aqueous nitric acid solution was prepared by adding 6 g HNO_3 to 97 mL DI water. Thereafter, 10 g of PEG was added to the solution and dissolved via the dropwise addition of 76 g TEOS. The formed colloidal solution was then stirred at 25 °C and 350 rpm until a clear solution was obtained (~15 min). Next, the required amount of ZrP or TiB, as well as CTAB, were added to the reaction mixture, and stirring was continued until complete dissolution was observed. The gelation of the solution

was performed at 40 °C without agitation for 10 h followed by aging under the same condition for 48 h. The particles were acidified with a 0.1 M HNO_3 solution and then washed 3 times with DI water for 5 h and then 3 times with ethanol for 5 h before drying for 3 days at 60 °C. The synthesized bimodal bare SiO_2 was named S4, whereas the bimodal TiO_2/SiO_2 and ZrO_2/SiO_2 were denoted as S5 and S6, respectively. To obtain the final porous materials from the fine powders, all the samples (S1–S6) were calcined in static air at 550 °C for 6 h with a heating ramp rate of 10 °C/min.

2.3. Adsorbent characterization

N_2 physisorption isotherms were obtained at 77 K on an automatic static volumetric adsorption system (Micromeritics 3Flex). Prior to measurements, samples were degassed at 250 °C in Micromeritics Smart VacPrep under vacuum for 12 h. The surface areas of the adsorbents were determined from the isotherms using the Brunauer-Emmett-Teller (BET) model, whereas non-local density functional theory (NLDFT) was used to determine the pore size distribution (PSD). X-ray photoelectron spectroscopy (XPS) was performed to determine the chemical composition of the samples on a Kratos Axis 165 photoelectron spectrometer with an aluminum X-ray source, while powder X-ray diffraction (XRD) using a step rate of 0.7°/min was performed on a PANanalytical X'Pert multipurpose X-ray diffractometer to identify the crystallinity of the samples. Zero diffraction silicon plates (SIL'TRONIX) were used for XRD to eliminate any background noise. Scanning electron microscopy (SEM) was performed on a Zeiss Merlin Gemini field emission microscope (FE-SEM). Energy dispersive spectroscopy (EDS) was collected on a Bruker 5030 X-Flash diffractometer using an accelerating voltage of 25 kV.

2.4. Adsorption isotherm measurements

The equilibrium adsorption capacities of the adsorbents at 25 °C were determined by running vapor adsorption isotherm experiments using benzene vapor as the adsorbate. A liquid benzene-filled reservoir was used as the source of the vapor. However, in other to properly collect the vapor isotherms, the benzene vapor was first purified using the freeze–thaw purification method. Prior to the vapor isotherm measurements, about 100 mg of the sample was degassed at 250 °C under vacuum for 6 h and then cooled to 25 °C, before being transferred to the Micromeritics 3Flex for isotherm measurements.

Nonlinear regression fittings were carried out to mathematically represent the benzene adsorption isotherm data. Different isotherm models such as dual-site Sips (DSS), linear combination of the Freundlich and dual-site Sips (FDSS), and BET models were used to obtain the best fit. All the isotherm models tested are described in Supporting Information.

2.5. Adsorption breakthrough experiments

To assess the dynamic performance of unimodal and bimodal silica adsorbents, breakthrough experiments were performed at 25 °C and 101 kPa in the glass column setup depicted in Fig. 1. The adsorption temperature was controlled by a K-type thermocouple, heating tape, and an Omega benchtop controller, while the flow rates were controlled by Brooks Instrument mass flow controllers. The column was packed with about 400 mg of the adsorbent and pretreated *in-situ* by degassing at 250 °C for 1 h under a 40 mL/min flow of N_2. Thereafter, the system was cooled to the adsorption temperature followed by temperature stabilization for about 15 min. The benzene vapor was carried over to the bed by passing a N_2 stream through a bubbler-saturator system filled with liquid benzene at a flow rate of 60 mL/min. The bed outlet concentration during adsorption was analyzed on-line by using a – BELMass quadrupole mass spectrometer with a mass range of 1–200 amu and minimum detection limit of < 1 ppm. In these

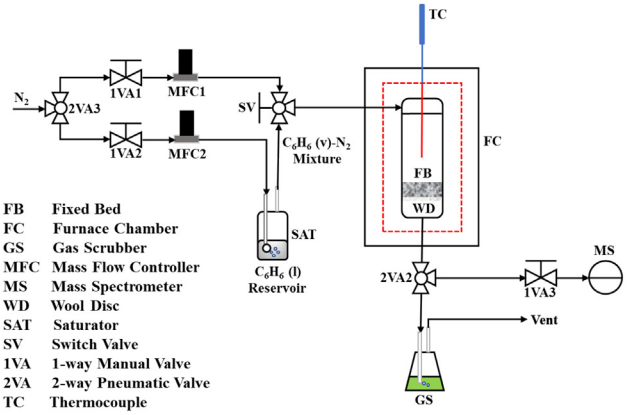

Fig. 1. Schematic of the adsorption breakthrough experiment.

measurements, the sensitivity was set at AUTO (1×10^{-11} A), emission at 1.0 mA, and the continuous secondary electron multiplier (C-SEM) at 800 V.

The dynamic adsorption capacity of benzene vapor was used as another performance metric and was calculated by using Eq. (1):

$$q_d = \frac{(F_{in}/24.8)(c_{in}/10^6)(t_{ads}/60)}{m_s} \tag{1}$$

where F_{in} (mL/min) was the inlet feed flow rate, c_{in} (465 ppm) was the benzene vapor bed inlet concentration, t_{ads} (s) was the time equivalent to the adsorption capacity of the bed, 24.8 (mL/mmol) is the gas molar volume at the adsorption dynamic experiment operating conditions (25 °C and 101 kPa), 10^6 (ppm) to convert from ppm to fraction, and 60 (s/min) to convert from min to s, and m_s (g) was the mass of the adsorbent sample loaded onto the column.

The saturator output volumetric flow rate was calculated by using Eq. (2): [28,29]

$$F_{in} = (P^0_{C_6H_6}/P_{N_2} + 1)F_{in,N_2} \tag{2}$$

where $P^0_{C_6H_6}$ is the benzene saturation vapor pressure at the operation temperature (25 °C) and P_{N_2} was the pressure of the carrier N_2, the value of which was set at the N_2 cylinder pressure gauge as 140 kPa. The benzene saturation vapor pressure, $P^0_{C_6H_6}$, was calculated using the Antoine equation given in Eq. (3):

$$P^0_{C_6H_6} = 10^{\left(6.88 - \frac{1196.76}{219.16+T}\right)} \tag{3}$$

From Eq. (3), the benzene saturation vapor pressure at 25 °C was calculated to be 12 kPa. Four different adsorption times, t_{ads} (s), were considered in this study, namely, $t_{0.1}$ (s), $t_{0.5}$ (s), $t_{1.0}$ (s), and t_{sto} (s). The stoichiometric adsorption time, t_{sto} (s), is the time equivalent to the stoichiometric (i.e., theoretical or total) adsorption capacity of the fixed bed and was calculated using Eq. (4):

$$t_{sto} = \int_0^\infty \left(1 - \frac{c_{out}}{c_{in}}\right) dt \tag{4}$$

All other times ($t_{0.1}$, $t_{0.5}$, and $t_{1.0}$) were obtained directly from the dynamic adsorption profiles.

To make an objective comparison between the adsorbents tested in this study, other than the use of q_d, partition coefficient (k_H), was also calculated from the breakthrough data by using Eq. (5):

$$k_H|_{BT-Level} = \frac{q_d|_{BT-Level}}{c_{out}|_{BT-Level}} \equiv \frac{q_d|_{BT-Level}}{c_{in} \times \left(\frac{c_{out}}{c_{in}}\right)\Big|_{BT-Level}} \tag{5}$$

The use of this equation was based on the dynamic adsorption data rather than equilibrium adsorption (isotherm) data. Moreover, it should be noted here that the terms in the Eq. (5) were evaluated at a

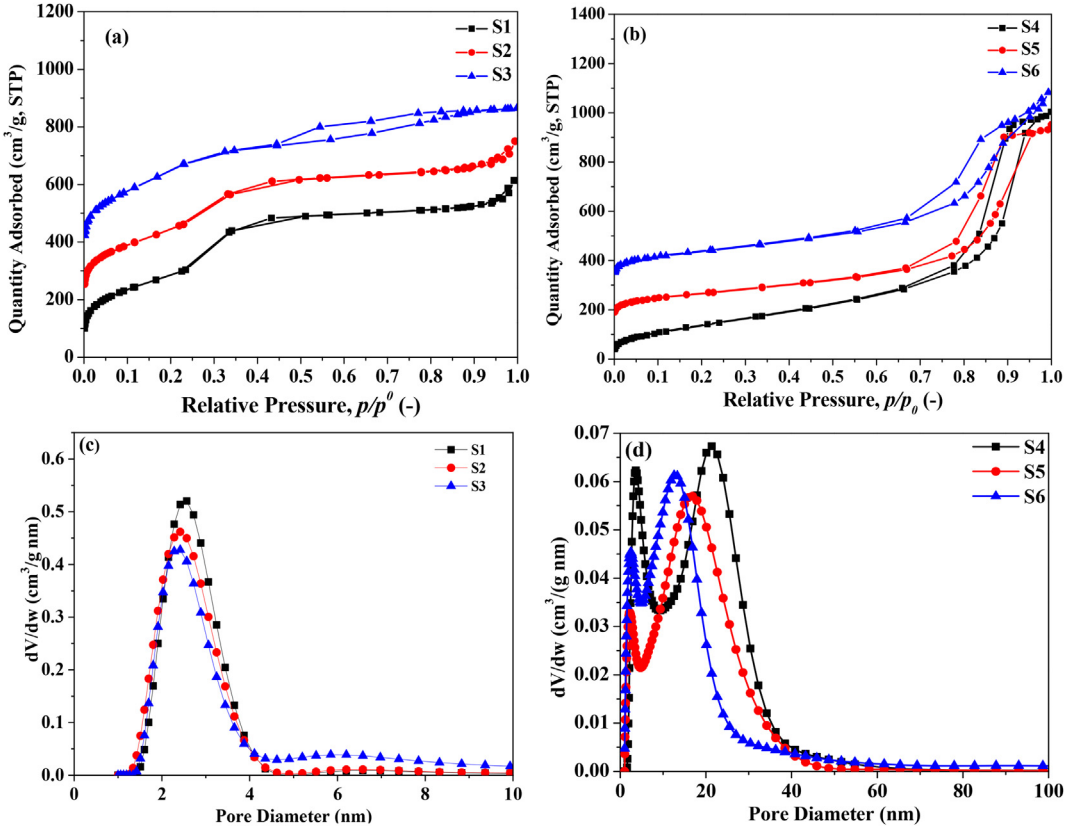

Fig. 2. N_2 physisorption isotherms and PSD profiles for (a-b) unimodal S1, S2, and S3, and (c-d) bimodal S4, S5, and S6 samples. S2 and S5 were shifted vertically upward by 150 units and S3 and S6 by 300 units.

particular breakthrough level (*BT-Level*), e.g., 10%, 50%, and 100% breakthroughs.

To fit the experimental data mathematically, mass, momentum, and energy balance equations were solved in gPROMS 5.1.1 (PSE Enterprise, United Kingdom). The partial differential equations (PDEs) and the corresponding initial and boundary conditions are included in Supporting Information. Moreover, the physical parameters were estimated using appropriate correlations in the literature, as noted in Supporting Information [30,31].

3. Results and discussion

3.1. Material characterization

The N_2 physisorption isotherms for the two sets of adsorbents are presented in Fig. 2. Whereas unimodal samples displayed a combination of types II and IV isotherms, bimodal samples showed a typical type IV isotherm. From Fig. 2a, for all three samples, the onset of multilayer coverage began at $p/p_o \sim 0.3$ with S3 showing type H4 hysteresis indicative of the presence of narrow slit-like pores in its structure [32]. As can be seen from Fig. 2b, for bimodal S4, S5, and S6, the first step corresponding to monolayer-multilayer adsorption in micropores occurred in $p/p_o \leq 0.6$ region, whereas filling of the large cage-like intercrystallite voids (mesopores) through capillary condensation took place in $p/p_o > 0.6$ region [17]. These isotherms also showed type H1 hysteresis, indicative of the presence of relatively large cylindrical pores [33].

Similarly, the PSD profiles shown in Fig. 2c revealed uniform pore sizes for unimodal S1, S2, and S3 adsorbents mainly in the range of 1.5–4 nm. On the contrary, the heterogeneity of the pores for bimodal samples was evident from Fig. 2d, with S4, S5, and S6 materials displaying small and large pores in the range of 1.5–6 and 12–20 nm, respectively. As also evident, for both unimodal and bimodal sets, the incorporation of TiO_2 and ZrO_2 resulted in reduction of pore size of the silica supports as a result of partial pore blockage, which is consistent with reported literature [27,34].

The summary of the corresponding textural properties estimated from N_2 physisorption isotherms is provided in Table 1. The BET surface areas of the unimodal adsorbents, S1 (1375 m^2/g), S2 (1254 m^2/g), and S3 (1241 m^2/g), were found to be higher than those of bimodal S4 (532 m^2/g), S5 (412 m^2/g), and S6 (483 m^2/g) adsorbents. The underlying cause of this difference was the presence of a larger number of small micropores in unimodal samples relative to the majorly mesoporous bimodal samples. In other words, it was due to the decrease in interior surface area as pore size increases [21]. The reduction in both surface area and pore volumes upon incorporation of TiO_2 and ZrO_2 was also evident from literature [17,34,35]. Another observation from these results was the higher total pore volume for bimodal S4, S5, and S6 samples (1.50, 1.20, 1.08 cm^3/g, respectively) relative to their

Table 1
Textural properties of adsorbents.

Sample	BET surface area (m^2/g)	NLDFT Pore volume (cm^3/g)		NLDFT pore diameter (nm)		Micropore (%)
		Micro.	Meso.	Micro.	Meso.	
S1	1375	0.08	0.92	1.7	2.6	8.0
S2	1254	0.15	0.68	1.4	2.4	18.1
S3	1241	0.32	0.56	1.5	2.3	36.4
S4	532	0.01	1.49	1.8	3.7, 22.0	0.7
S5	412	0.02	1.18	1.3	2.3, 19.5	1.7
S6	483	0.03	1.05	1.5	2.4, 17.5	2.7

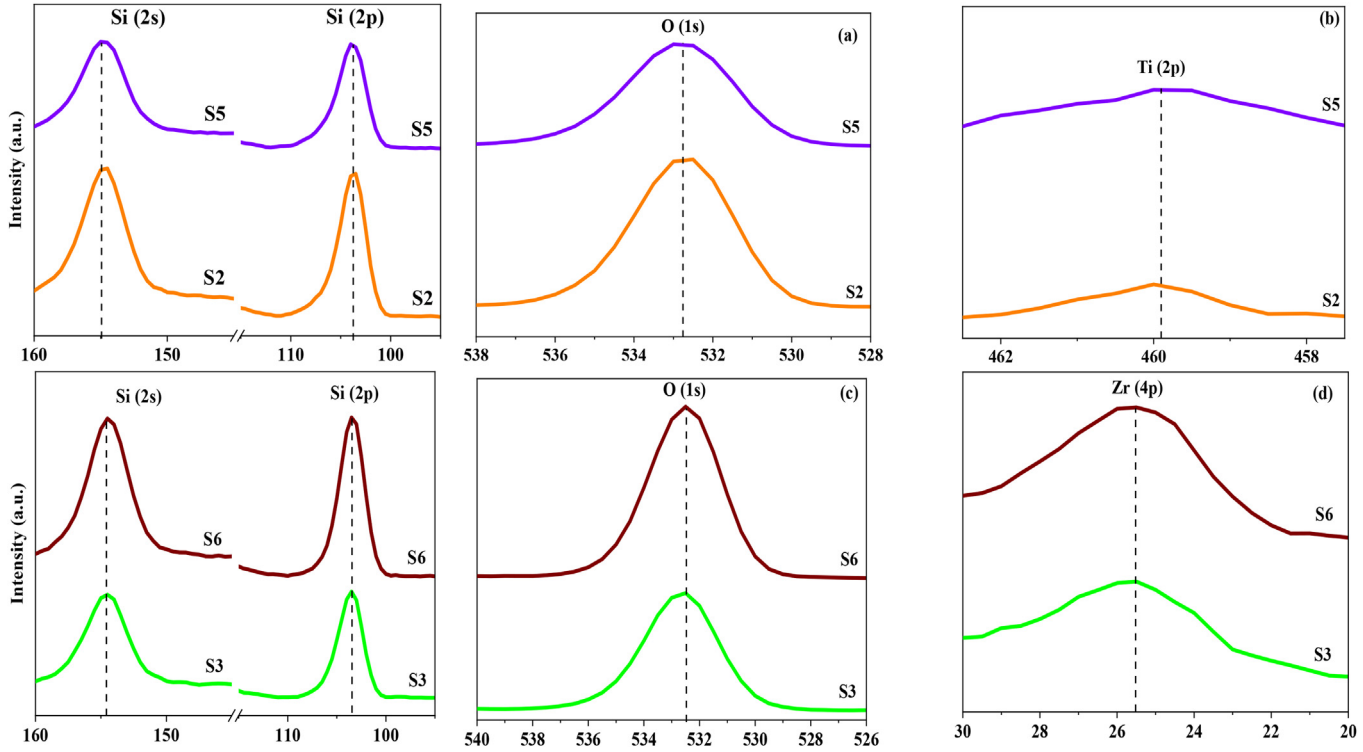

Fig. 3. XPS spectra for MMO samples: (a) Si and O for S2 and S5, (b) Ti for S2 and S5, (c) Si and O for S3 and S6, and (d) Zr for S3 and S6.

unimodal S1, S2, and S3 counterparts (1.00, 0.83, 0.88 cm^3/g, respectively) due to their large mesopore volume. This trend was expected as the main goal of making such bimodal materials was to enhance mesoporosity which in turn improves the adsorption kinetics.

The XPS results are illustrated in Fig. 3 while the elemental composition of the MMOs are listed in Table 2. Two characteristic peaks of Si 2p and 2s were observed at 103 and 154 eV, respectively whereas one distinct 1s O peak was detected at 535 eV. For the S2 and S5 materials, Ti 2p was detected around 460 eV while Zr 4p was detected around 25 eV. The XPS survey spectra of the samples are also provided in Fig. S1, Supporting Information.

Metal loading was calculated by using metal to silica ratio. The amounts of O and Si were nearly constant in all the materials thereby showing uniformity in the composition of the SiO_2 bare supports for the unimodal and the bimodal adsorbents. Likewise, Ti in S2 (0.93 atom %) and S5 (1.50 atom %), and Zr in S3 (1.32 atom %) and Zr (1.20 atom %) in S6 were reasonably close, thereby showing similarity in the amounts of TiO_2 and ZrO_2 doped on the silica supports. The Ti or Zr weight loading was estimated to be approximately 3–4 wt.% on all the adsorbent materials, which showed uniformity in loading of the bare silicas.

The high-angle (10–90°) XRD patterns of the adsorbent materials are shown in Fig. 4. Clearly, all the materials depicted the characteristic less-crystalline nature of UVM-7 silica [22]. Furthermore, the patterns showed at least one strong but broad diffraction peak around $2\theta = 23°$.

Table 2
Elemental composition and metal loading of the samples determined by XPS.

Sample	S (atom %)	O (atom %)	Ti or Zr (atom %)	Ti or Zr loading (wt. %)
S1	44	56	–	–
S2	42	57	0.93	3
S3	44	54	1.32	3
S4	44	56	–	–
S5	42	56	1.50	3
S6	42	56	1.20	4

This broadness of the peaks could be due to the small size of the particles in accordance with Scherrer equation. Moreover, since peak intensity and position were essentially identical for bare and doped MMOs, it was conclusive that the incorporation of TiO_2 or ZrO_2 on the SiO_2 supports did not alter the crystal structure of the silica supports.

The materials' surface topographies and particle sizes were assessed by both low and high magnification SEM, as shown in Fig. 5. As can be seen, the unimodal bare silica (Fig. 5a, b) was of nearly amorphous structure and contained a rough surface topography with particle conglomerates of ~2 μm in diameter. Meanwhile, the diameter of the agglomerated macroparticles exceeded 100 μm. Upon loading the unimodal silica with titanium oxide, the macroparticles maintained their 100 μm diameters and rough surface topographies (Fig. 5c), however, spherical titanium oxide agglomerations – whose structure agrees with literature [17] – were observed at high magnification (Fig. 5d). The individual titanium oxide particles were ~500 nm in diameter. In the unimodal silica loaded with zirconium oxide, low-magnification SEM revealed a distinct change in the particle structure (Fig. 5e). Namely, modifying the silica with zirconium rendered the particulate surface less coarse and produced distinct crystalline planes. This being the case, high-magnification SEM revealed that – similar to the titanium oxide loaded sample – the zirconium oxide loading produced agglomerations of particulate which were ~2 μm in length (Fig. 5f).

Moving on to the bimodal samples, low magnification SEM revealed a much smoother texture in the bare silica as well as macropores which were between 2 and 3 μm (Fig. 5g). On the other hand, similar particle roughness and size to the unimodal silica were observed under high magnification (Fig. 5h). As evident, however, the differences in particle structure did lead to variance upon oxide loading from the unimodal silica. After loading titanium oxide, for example, the silica developed distinct crystal planes (Fig. 5i). Moreover, it should also be noted that, while the individual oxide particles were similar in size to those on the unimodal silica, they were not agglomerated. A similar effect was also observed in the zirconium oxide particles at high magnification (Fig. 5l). The loss in particle agglomeration for both samples can easily be attributed to the macropores in bimodal silica – which allowed more

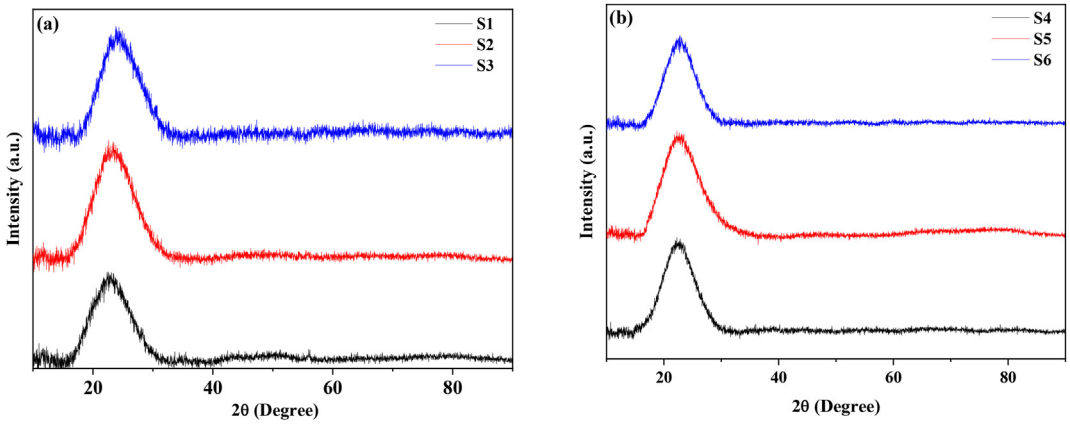

Fig. 4. High-angle XRD patterns of (a) S1, S2 and S3, and (b) S4, S5 and S6.

space for nanoparticle growth during calcination – thereby eliminating catenation between individual oxides. This being the case, it should be noted that, unlike the unimodal S1, loading zirconium oxide did not produce a crystalline phase (Fig. 5k). Instead, the silica retained its coarse, amorphous, structure. Similarly, the differences in crystallinity can likely be attributed to the density of the doping metal oxide.

The elemental maps for the oxide modified silicas are shown in Fig. 6. In both unimodal S2 and S3 samples (Fig. 6a–f), the elemental maps of both metals overlapped nearly perfectly with the silica maps, indicating an even dispersion of oxides across the macroparticle surface. This was in agreement with the SEM micrographs, which clearly showed clusters of oxide nanoparticles contained on the surface. A similar dispersion was also observed in the bimodal silica samples (S5 and S6 samples), however, there were slight differences between the titania (Fig. 6g–i) and zirconia (Fig. 6j–l) modified silicas. Specifically, clusters of oxides were observed in the latter – which can be attributed to zirconium high density – while the former exhibited a more even dispersion across the silica particles. In general, as clear from the maps,

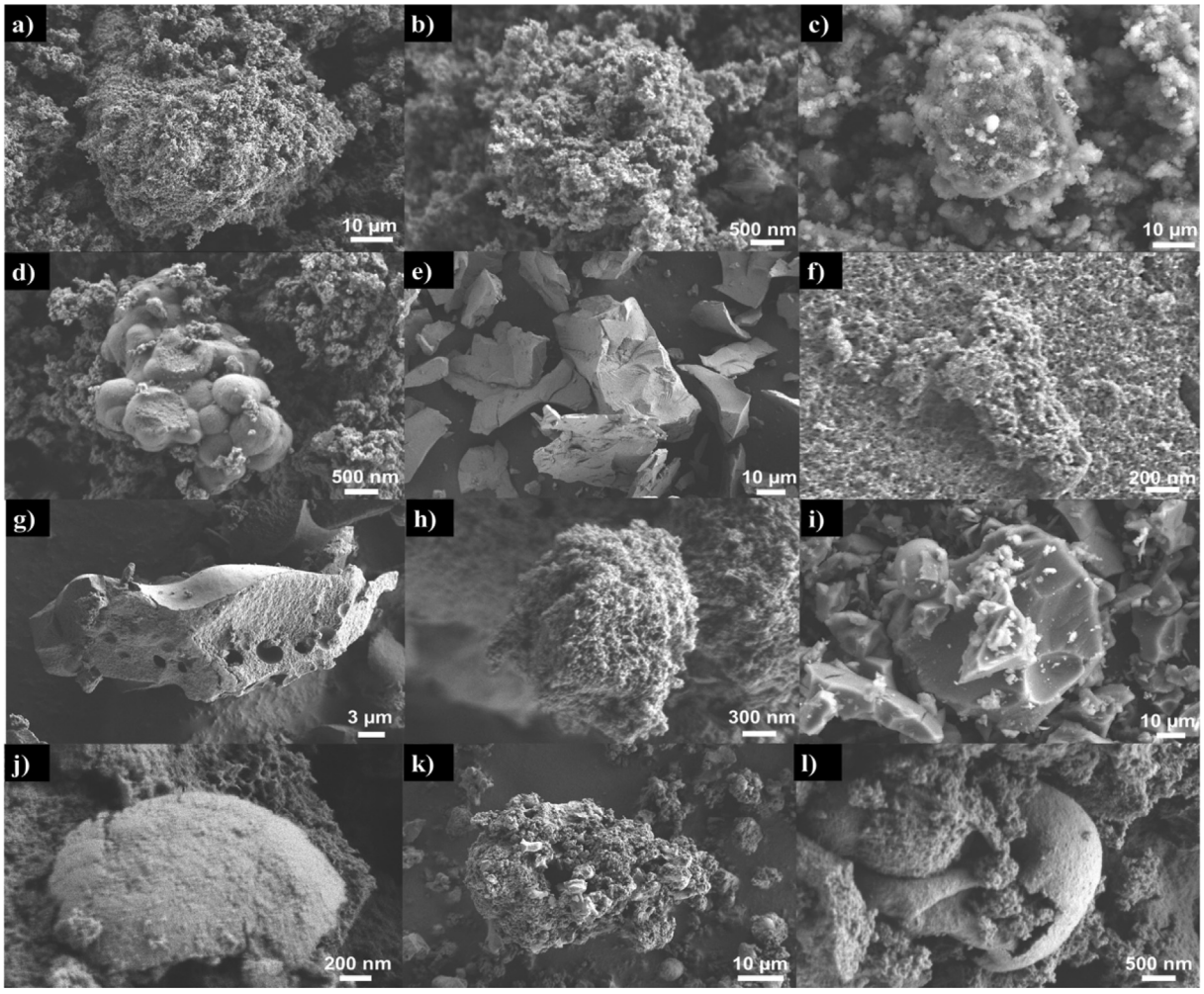

Fig. 5. Low and high magnification SEM images of (a-b) S1, (c-d) S2, (e-f) S3, (g-h) S4, (i-j) S5, and (k-l) S6.

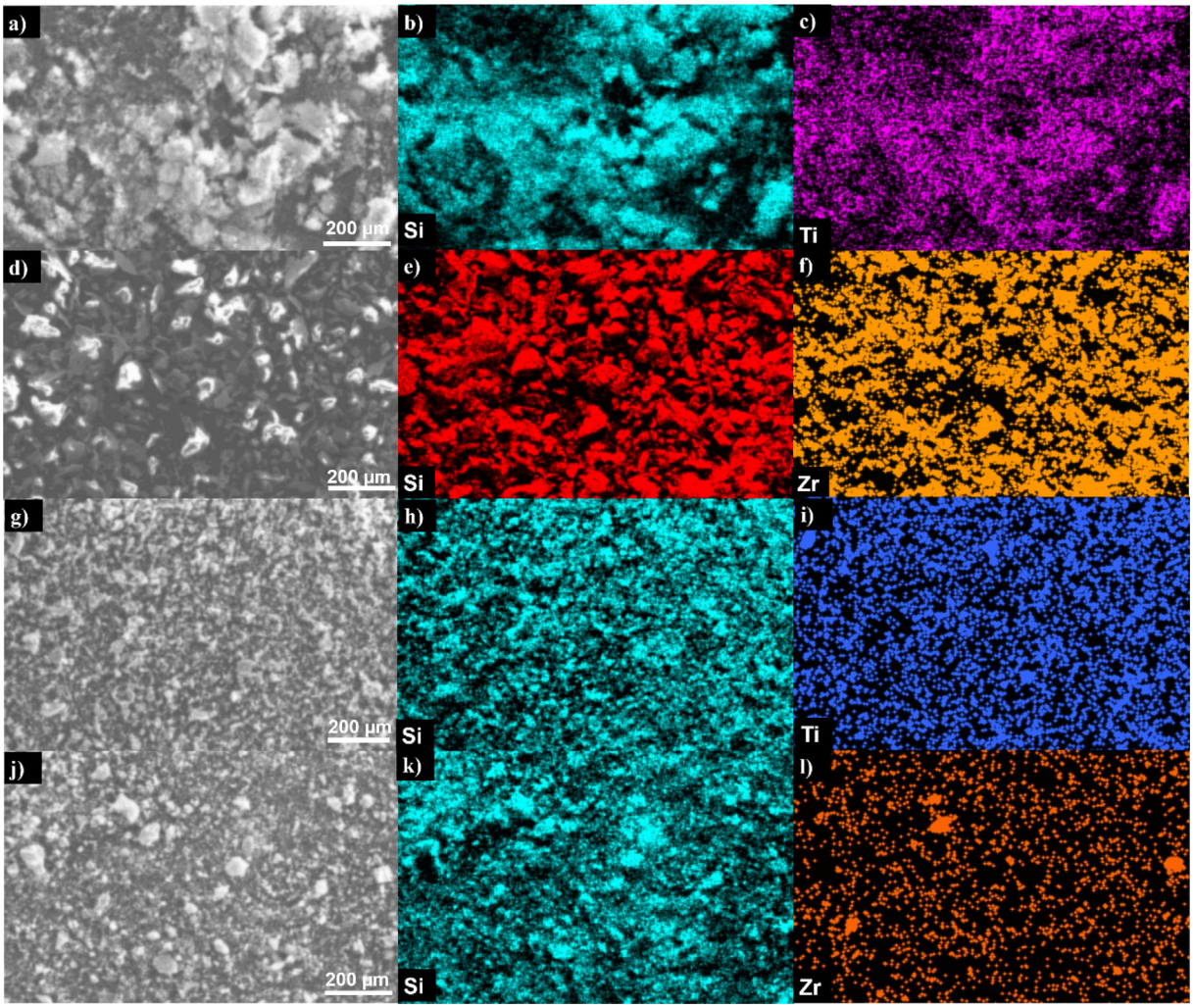

Fig. 6. Elemental maps of (a-c) S2, (d-f) S3, (f-h) S5, and (j-l) S6.

both oxides loaded effectively on the unimodal and bimodal bare silicas, however, the high density of zirconium led to a less even dispersion between macroparticles in the bimodal sample.

The EDS spectra of the materials are displayed in Fig. 7. These spectra clearly showed the bulk elemental composition of the samples. In all the materials, Si Kα and O Kα were observed at 1.7 and 0.6 keV, respectively. Characteristic peaks of Ti and Zr were also annotated in the figure. As expected, the intensities of Ti and Zr in the MMO samples were small relative to those of Si and O because of the small amounts of Ti and Zr precursors used for the doping. These small amounts were earlier attested to in the XPS analysis.

3.2. Benzene adsorption isotherms

The benzene vapor adsorption isotherms for the six adsorbents obtained at 25 °C are shown in Fig. 8. From Fig. 8a, the unimodal S1 and S2 samples depicted three distinct regions of adsorption viz: $0 < p/p_o < 0.15$, $0.15 < p/p_o < 0.75$ and the higher, near benzene

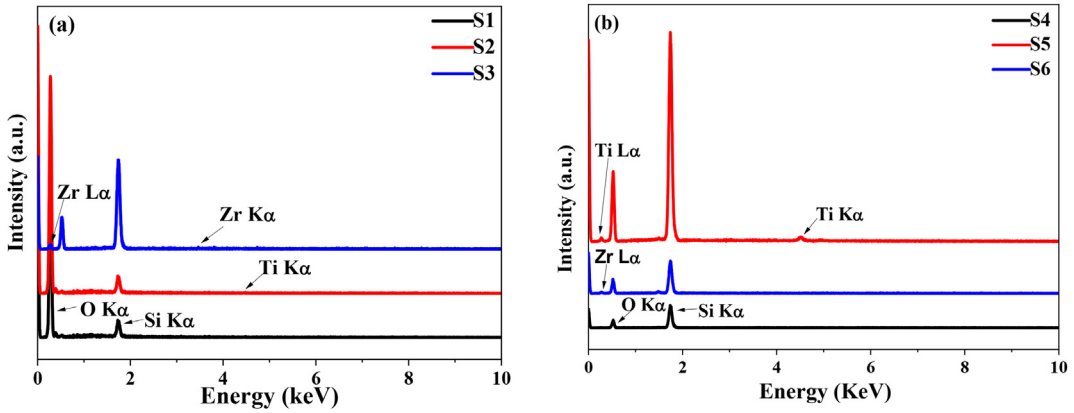

Fig. 7. EDS spectral of (a) S1, S2 and S3, and (b) S4, S5 and S6.

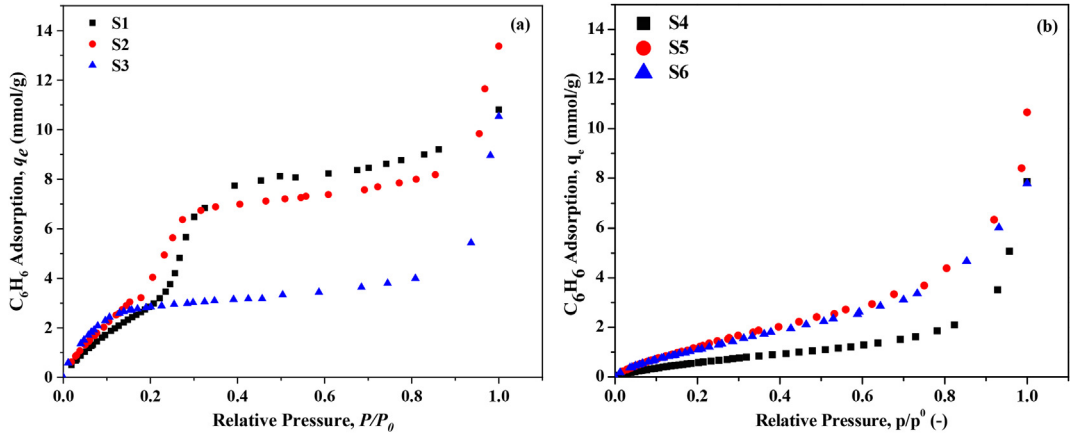

Fig. 8. Benzene adsorption isotherms for (a) unimodal S1, S2, and S3, and (b) bimodal S4, S5, and S6 adsorbents at 25 °C.

saturation-vapor pressure adsorption region. However, S3 only depicted adsorption in the first and the last regions. This indicates that S1 and S2 are more heterogeneous than S3. In the first and the lower region, $0 < p/p_o < 0.15$, all the unimodal adsorbents exhibited a similar benzene equilibrium adsorption behavior, whereas in the intermediate region, $0.15 < p/p_o < 0.75$, S1 and S2 had higher benzene equilibrium adsorption capacity than S3 adsorbent. At the tail end of equilibrium adsorption, near the benzene saturation vapor pressure, S2 and S3 isotherms were slightly steeper than S1's isotherm and thus equivalently showed slightly higher equilibrium adsorption than S1. It is evident from Fig. 8b that the bimodal S4, S5, and S6 all displayed similar shapes of adsorption isotherms describable by the BET monolayer-multilayer model, but with S4 having smaller benzene equilibrium adsorption capacity throughout the entire pressure range. Overall, all of the adsorbents exhibited a relatively large adsorption uptake close to the benzene saturation vapor pressure. However, it is worth noting here that adsorption up to the benzene saturation vapor pressure, 12.7 kPa, was hardly attained due to condensation formation.

Moreover, between the two groups of adsorbents tested in this work, the unimodal MMOs were at least 50% higher in equilibrium adsorption capacity than the bimodal counterparts at the lower absolute pressure of $0 \leq p/p_o \leq 0.2$ (the first adsorption region) on account of their higher surface areas. For instance, at $p/p_o \sim 0.2$, unimodal adsorbents exhibited an uptake capacity of approximately 3.0 mmol/g compared to the 1.0 mmol/g (S4) and 1.5 mmol/g (S5 and S6) of the bimodal adsorbents. Similarly, in the intermediate adsorption region, $0.2 < p/p_o < 0.75$, S1 and S2 maintained a similar trend over S4 and S5, respectively, while S3 and S6 displayed adsorption capacities of about 4 and 6 mmol/g, respectively. Interestingly, while both sets of MMOs showed similar adsorption performances at the lower and upper adsorption regions, the Ti-doped silica adsorbents (S2 and S5) showed higher adsorption capacities over their Zr-doped analogous (S3 and S6) in the intermediate adsorption region, especially in the case of unimodal adsorbents. Taking into account similar textural properties of S2 and S3 as shown in Table 1, the only plausible explanation for this behavior is a higher number of active sites on the S2 adsorbent as compared with S3 stemming from the former's higher lower density which gave rise to better dispersion on the silica support [14]. On the contrary, the slightly higher adsorption capacity of S5 over S6 could be attributed to its relatively larger mesopore volume, as also reported previously [21,36]. Moreover, as adsorption approached benzene saturation relative pressure (> 0.75), both unimodal and bimodal sets depicted large equilibrium adsorption capacities ~13 and 11 mmol/g, respectively. As expected, titania and zirconia doping resulted in higher uptakes than that of the bare silica in both cases, despite reduction in surface area, owing to increased number of active sites and increased affinity toward benzene molecules [16,35]. In other words, besides lower adsorption sites, the weak hydrogen bond between the silanol groups on the silica surface and the benzene delocalized pi electrons is responsible for lower adsorption capacity of bare silica samples [1,16]. As reported by Jan et al. [37], most of the materials investigated for benzene adsorption so far exhibit capacities around 10 mmol/g at $p/p_o \sim 1$, thus the obtained capacities reported here are comparable to literature data, albeit some MOFs and activated carbons with capacities as high as ~20 mmol/g have been reported [38,39].

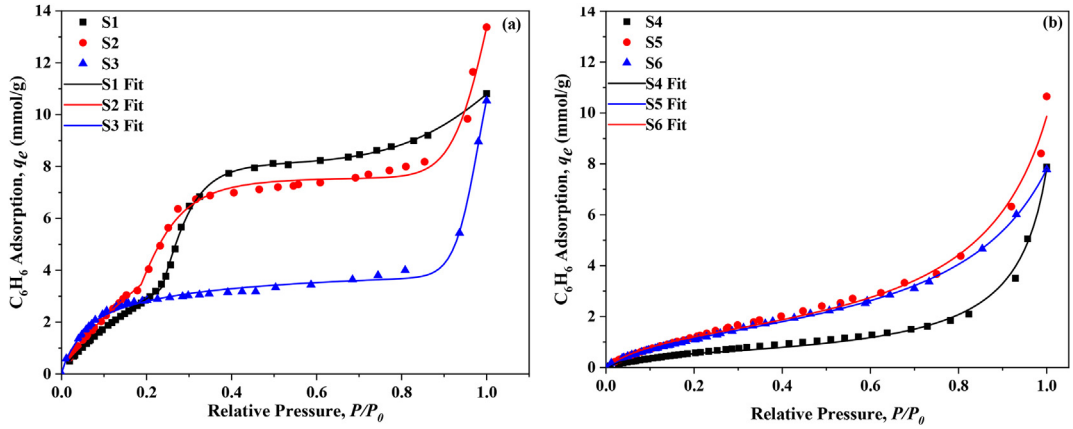

Fig. 9. Benzene-adsorbents equilibrium adsorption isotherms fittings (a) for S1, S2, and S3, and (b) for S4, S5, and S6: Symbols are the experimental data points while lines are the corresponding fittings.

3.3. Benzene adsorption isotherm fittings

The mathematical fittings of the isotherms are shown in Fig. 9. Due to the apparent complexity in the shapes of the unimodal adsorbent isotherms, especially those of S1 and S2, two isotherm models were compared in fitting the isotherms, namely, DSS, BET, and FDSS models. Between these isotherm models, the FDSS model was found to give the best fit for the unimodal adsorbent isotherms, as evident in Fig. 9a. On the other hand, for the bimodal adsorbent isotherms (Fig. 9b), it was very clear at first glance that the BET isotherm model would give the best fits, and thus was the only model used. It should be noted here that the fitted isotherms using the FDSS model for the unimodal and the BET model for the bimodal adsorbents were the only ones presented in Fig. 9. The isotherm fitting parameters and statistical values can be found in Tables S1–S3, Supporting Information. These fitting parameters were used in the simulation of breakthrough concentration profiles. In all cases, $R^2 \geq 0.99$, indicating that the adsorbents could all be described by the respective isotherm models.

3.4. Dynamic adsorption breakthrough profiles

The results of the dynamic adsorption experiments carried out on all the six materials are shown in Fig. 10. In general, and in agreement with their higher equilibrium capacities, the unimodal samples displayed longer breakthrough and saturation times compared to the bimodal analogues, as a result of their higher surface areas [40]. Likewise, within similar pore size distributions, the titania and zirconia-doped MMOs showed longer breakthrough and saturation times than the corresponding bare silicas, a trend that is attributable to increased number of active sites and affinity toward adsorbate molecules, as discussed earlier [21].

Adsorption front steepness is another important feature of every adsorption breakthrough profile. It is an indication of the rate of mass transfer to the adsorbent active sites, thereby providing a facile approach for estimation of the mass transfer and diffusion parameters. Comparison of the concentration profiles revealed that bimodal adsorbents (Fig. 10b) exhibited sharper wavefronts than those of unimodal adsorbents (Fig. 10a) on the account of their hierarchical pore structure and thus less mass transfer resistances. As indicated in Table 3, the temporal values of the mass transfer zone (MTZ) estimated in the time interval of $t_{1.0} - t_{0.1}$ were 1838, 3405, and 3010 s for unimodal S1, S2, and S3 compared to 1175, 1518, and 2110 s for bimodal S4, S5, and S6, indicative of faster kinetics for the latter samples. In fact, this highlights that diffusion in the adsorbent particles was the major mass transfer resistance in adsorption column. Moreover, across pore size distributions, the unimodal lower micro-mesoporous adsorbents exhibited higher dynamic adsorption capacity than that of bimodal upper micro-mesoporous adsorbents, with dynamic adsorption capacities (q_d) of 9.89, 10.94, and 10.81 mmol/g for S1, S2, and S3, respectively, relative to 6.88, 8.68, and 8.91 mmol/g for S4, S5, and S6, respectively. Moreover, the dynamic adsorption capacities calculated at t_{sto} and $t_{1.0}$ were about 55% and 95% of their corresponding equilibrium values, which further implied that $t_{1.0}$ is a better representative of the dynamic adsorption capacities.

Another observation from these results is the effect of metal incorporation on the sharpness of the wavefronts. As clearly evident, titania and zirconia-doped MMOs gave rise to broader fronts than the bare silica samples, especially in the case of unimodal materials which could be due to reduced pore size or partial blockage of the pores after metal incorporation.

Table 4 shows the values of the partition coefficients calculated for the materials tested in this study at different breakthrough times. Each corresponding dynamic adsorption capacity was also included for comparison. Generally, it was observed that k_H was directly proportional with the adsorption capacity at each breakthrough level. For instance, among the unimodal samples, S2 showed the highest k_H at 50 and 100% breakthrough levels, followed by S3. The swap observed between S2 (k_H = 1.55 mmol/g/μM) and S3 (k_H = 1.74 mmol/g/μM) at 10% breakthrough level was in agreement with the intersection seen in their breakthrough profiles around 10% breakthrough and similarly isotherm profile. However, among the bimodal samples, S6 showed the highest k_H at all breakthrough levels, followed by S2. These trends depend mainly on the properties of the materials.

3.5. Investigation of benzene adsorption kinetics

To assess the kinetics of benzene adsorption on the MMOs, the breakthrough profiles were modeled and mass transfer parameters were estimated. The experimental and predicted breakthrough profiles are depicted in Fig. 11. For the unimodal adsorbents, the deviation observed in S1 and S2 breakthrough fittings (Fig. 11a, b) could most probably be due to the use of the less fit DSS isotherm model rather than the perfect fit FDSS model in the isotherm fittings. This choice was due to the computational time involved in the breakthrough fittings, thus resulting in a trade-off between isotherm fitting and breakthrough computational time. Conversely, for the bimodal adsorbents the breakthrough fronts were all well fitted by the dynamic adsorption model. In general, the adsorption breakthrough profiles were all satisfactorily fitted as depicted in Fig. 11. This is also easily seen by the values of their statistical error measurements, R^2, shown in Table S6, Supporting Information. For most cases $R^2 \geq 0.95$, which implies that the simulated breakthrough fronts accurately predicted the measured profiles.

The parameter estimation carried out on the gPROMS platform was

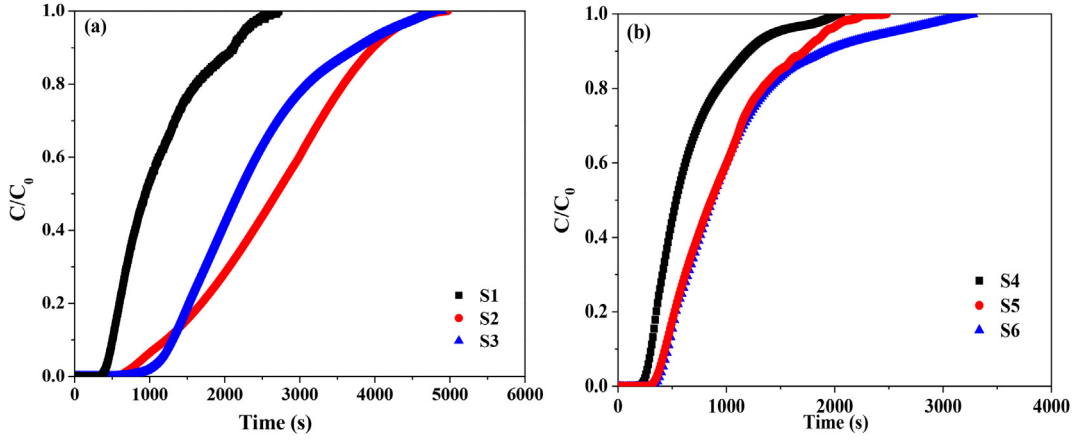

Fig. 10. Benzene-adsorbents experimental breakthrough profiles (a) for S1, S2, and S3, and (b) for S4, S5, and S6.

Table 3
Adsorbents dynamic adsorption data obtained from breakthrough profiles.

Sample	$t_{0.1}$	$t_{0.5}$	$t_{1.0}$	t_{sto}	MTZ	q_e	$q_{d,0.1}$	$q_{d,0.5}$	$q_{d,1.0}$	q_{sto}
	(s)	(s)	(s)	(s)	(s)	(mmol/g)	(mmol/g)	(mmol/g)	(mmol/g)	(mmol/g)
S1	455	920	2080	1068	1838	10.05	1.50	3.05	9.89	5.28
S2	927	2650	4332	2671	3405	11.71	3.13	8.95	10.94	6.66
S3	1118	2105	4218	2333	3010	11.25	3.51	6.61	10.81	6.05
S4	270	510	1455	660	1175	7.25	1.93	3.65	6.88	3.12
S5	392	945	1910	957	1518	9.31	2.96	7.14	8.68	3.59
S6	405	955	2515	1040	2110	8.95	3.07	7.24	8.91	4.51

Table 4
Adsorbents performance based on the values of their partition coefficients.

Sample	$t_{0.1}$	$t_{0.5}$	$t_{1.0}$	$q_{d,0.1}$	$k_{H,0.1}$	$q_{d,0.5}$	$k_{H,0.5}$	$q_{d,1.0}$	$k_{H,1.0}$
	(s)	(s)	(s)	(mmol/g)	(mmol/g/μM)	(mmol/g)	(mmol/g/μM)	(mmol/g)	(mmol/g/μM)
S1	455	920	2080	1.50	0.74	3.05	0.31	9.89	0.49
S2	927	2650	4332	3.13	1.55	8.95	0.89	10.94	0.54
S3	1118	2105	4218	3.51	1.74	6.61	0.66	10.81	0.53
S4	270	510	1455	1.93	0.96	3.65	0.36	6.88	0.34
S5	392	945	1910	2.96	1.47	7.14	0.71	8.68	0.43
S6	405	955	2515	3.07	1.52	7.24	0.72	8.99	0.45

used to determine the axial dispersion coefficient (D_{ax}), effective pore diffusivity (D_{eff}), and film mass transfer coefficient (k_f) values, as tabulated in Table 5. As can be inferred from these data, D_{ax} and D_{eff} were all higher for bimodal adsorbents compared to the unimodal consituents. We could also observe that the values of k_f were relatively equal across each group of the adsorbents. Similarly, the overall mass transfer coeffcients (k), estimated from Eq. S12b, Supporting Information, were approximately one order of magnitude higher for S5 and S6 (0.45 and 0.41 s^{-1}, respectively) than for S2 and S3 (0.03 and 0.04 s^{-1}, respectively). The higher values of D_{ax} for the bimodal adsorbents relative to the corresponding unimodal materials could be attributed to higher interparticle diffusion. However, for D_{eff}, the trend

Table 5
Estimated mass transfer parameters.

Sample	$D_{ax} \times 10^5$ (m^2/s)	$D_{eff} \times 10^3$ (m^2/s)	k_f (m/s)	k (s^{-1})
S1	0.51	0.35	0.49	0.08
S2	0.49	0.22	0.41	0.03
S3	0.55	0.25	0.45	0.04
S4	1.35	3.50	0.30	0.58
S5	1.25	1.87	0.29	0.45
S6	1.65	1.65	0.32	0.41

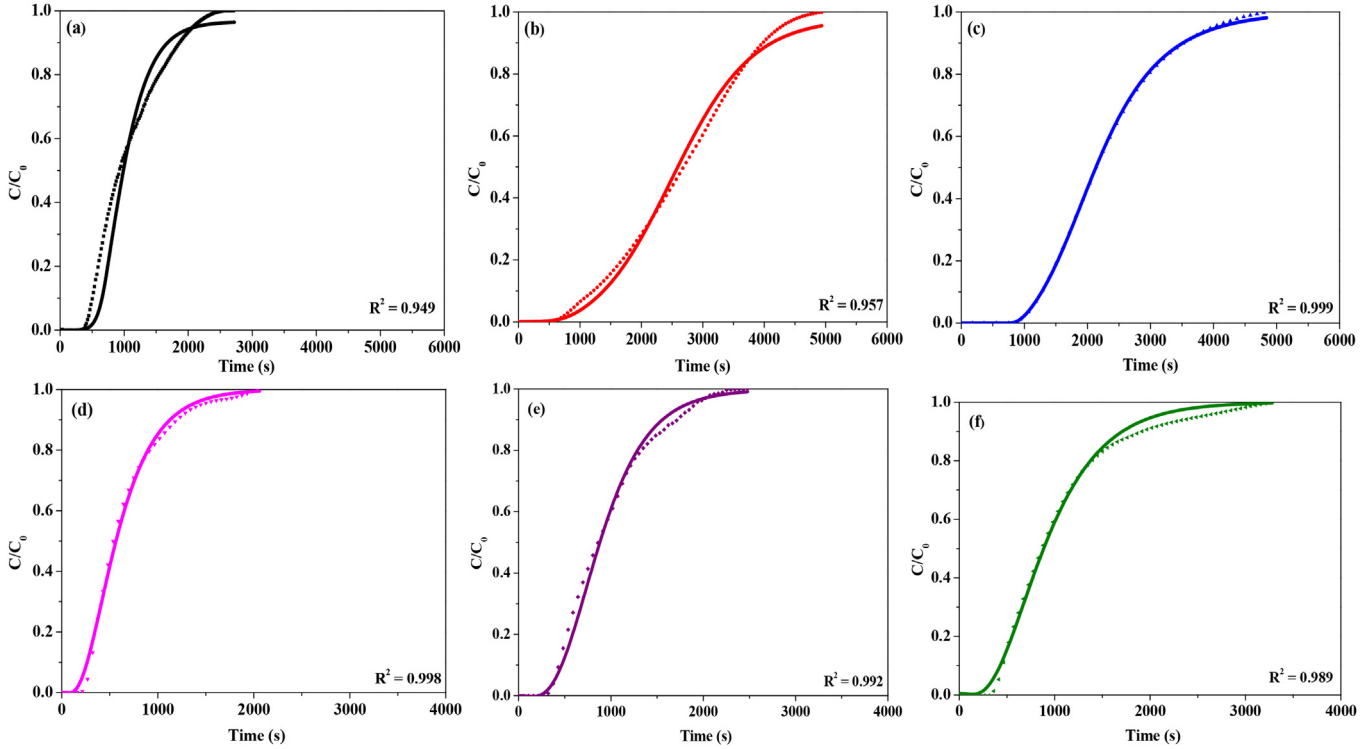

Fig. 11. Benzene-adsorbents breakthrough curves fittings (a–c) for S1, S2, and S3, and (e, f) for S4, S5, and S6. Symbols are the experimental data points while lines are the corresponding fittings.

observed could be readily correlated to the difference in their pore network [41]. Specifically, the bimodal adsorbents' increased pore diameters reduced the adsorbate's diffusional resistance and enhanced the mass transfer rate, and hence showed higher overall mass transfer coefficients (k).

4. Conclusions

In this work, we demonstrated the efficacy of novel bimodal silica-based MMOs in abatement of benzene vapor with both high equilibrium capacity and fast kinetics. Two sets of MMO adsorbents were prepared using unimodal and bimodal silicas doped with similar amounts of Ti and Zr. Analysis of N_2 physisorption isotherms revealed distinct differences in the textural properties of these two sets, with unimodal samples exhibiting approximately three-fold higher surface area and micropore volume than those of the corresponding bimodal samples. On the contrary, bimodal adsorbents displayed large mesopore volumes on the order of 1.17–1.26 cm^3/g. From the benzene vapor adsorption isotherm measurements at 25 °C, unimodal samples were found to exhibit relatively higher equilibrium uptakes than those of their bimodal analogues, particularly in the low-pressure range, on the account of their higher surface area. However, as the benzene pressure increased, all the adsorbents served equally well for adsorbing benzene vapor. These adsorption data also indicated more positive role of titania in improving benzene adsorption capacity that zirconia. To verify the better dynamic adsorption performance of bimodal adsorbents, breakthrough tests were carried out and the results confirmed sharper wavefronts and shorter MTZ lengths for these adsorbents relative to unimodal samples as a result of their larger pores which facilitated transport of benzene molecules and reduced the intraparticle mass transfer resistance. The mass transfer coefficient for unimodal Ti-doped (S2) and Zr-doped (S3) MMOs were estimated to be 0.03 and 0.04 s^{-1}, respectively, whereas under the same conditions, the values were 0.45 and 0.41 s^{-1} for the corresponding bimodal S5 and S6, respectively. Overall, the results of this study highlight that increasing the mesoporosity of a micro-mesoporous silica support is a facile and effective approach for developing MMO adsorbents that not only show high adsorption capacity but also fast kinetics for purification of benzene-lean streams.

Declaration of Competing Interest

The authors declare that they have no known competing financial interests or personal relationships that could have appeared to influence the work reported in this paper.

Acknowledgment

The authors thank the National Science Foundation (NSF CBET-1802049) for financially supporting this project.

Appendix A. Supplementary data

Supplementary data to this article can be found online at https://doi.org/10.1016/j.cej.2020.125273.

References

[1] L. Zou, Y. Luo, M. Hooper, E. Hu, Removal of VOCs by photocatalysis process using adsorption enhanced TiO_2-SiO_2 catalyst, Chem. Eng. Process. Process Intensif. 45 (2006) 959–964, https://doi.org/10.1016/j.cep.2006.01.014.
[2] C. Liaud, N.T. Nguyen, R. Nasreddine, S. Le Calvé, Experimental performances study of a transportable GC-PID and two thermo-desorption based methods coupled to FID and MS detection to assess BTEX exposure at sub-ppb level in air, Talanta 127 (2014) 33–42, https://doi.org/10.1016/J.TALANTA.2014.04.001.
[3] L.F. Liotta, Catalytic oxidation of volatile organic compounds on supported noble metals, Appl. Catal. B Environ. 100 (2010) 403–412, https://doi.org/10.1016/j.apcatb.2010.08.023.
[4] O. US EPA, Technical Overview of Volatile Organic Compounds, (n.d.).
[5] A. Krishnamurthy, B. Adebayo, T. Gelles, A. Rownaghi, F. Rezaei, Abatement of gaseous volatile organic compounds: a process perspective, Catal. Today 2 (2019) 1–20, https://doi.org/10.1016/j.cattod.2019.05.069.
[6] A.J. McMichael, Carcinogenicity of benzene, toluene and xylene: epidemiological and experimental evidence, IARC Sci. Publ. (1988) 3–18.
[7] T. Gelles, A. Krishnamurthy, B. Adebayo, A. Rownaghi, F. Rezaei, Abatement of gaseous volatile organic compounds: a material perspective, Catal. Today 2 (2019) 1–16, https://doi.org/10.1016/j.cattod.2019.06.017.
[8] L.-J. Hsu, C.-C. Lin, Removal of methanol and 1-butanol from binary mixtures by absorption in rotating packed beds with blade packings, Chem. Eng. J. 168 (2011) 190–200, https://doi.org/10.1016/J.CEJ.2010.12.062.
[9] K.-C. Huang, Z. Zhao, G.E. Hoag, A. Dahmani, P.A. Block, Degradation of volatile organic compounds with thermally activated persulfate oxidation, Chemosphere 61 (2005) 551–560, https://doi.org/10.1016/J.CHEMOSPHERE.2005.02.032.
[10] R. Gong, & Tim, C.C. Keener, A Qualitative Analysis of the Effects of Water Vapor on Multi-Component Vapor-Phase Carbon Adsorption, Air Waste. 43 (1993) 864–872. doi:10.1080/1073161X.1993.10467169.
[11] Y. Liu, X. Feng, D. Lawless, Separation of gasoline vapor from nitrogen by hollow fiber composite membranes for VOC emission control, J. Memb. Sci. 271 (2006) 114–124, https://doi.org/10.1016/J.MEMSCI.2005.07.012.
[12] E. Auer, A. Freund, J. Pietsch, T. Tacke, Carbons as supports for industrial precious metal catalysts, Appl. Catal. A Gen. 173 (1998) 259–271, https://doi.org/10.1016/S0926-860X(98)00184-7.
[13] C.J. Geankoplis, Transport Processes and Unit Operations, Third, P T R PRENTICE-HALL, n.d.
[14] L. Seifi, A. Torabian, H. Kazemian, G.N. Bidhendi, A.A. Azimi, S. Nazmara, M. AliMohammadi, Adsorption of BTEX on surfactant modified granulated natural zeolite nanoparticles: parameters optimizing by applying taguchi experimental design method, CLEAN - Soil Air Water. 39 (2011) 939–948, https://doi.org/10.1002/clen.201000390.
[15] R. Navarro Amador, L. Cirre, M. Carboni, D. Meyer, BTEX removal from aqueous solution with hydrophobic Zr metal organic frameworks, J. Environ. Manage. 214 (2018) 17–22, https://doi.org/10.1016/j.jenvman.2018.02.097.
[16] S. Sato, R. Takahashi, T. Sodesawa, S. Tanaka, K. Oguma, K. Ogura, High-surface-area SiO_2-ZrO_2 prepared by depositing silica on zirconia in aqueous ammonia solution, J. Catal. 196 (2000) 190–194, https://doi.org/10.1006/jcat.2000.3027.
[17] D. Ortiz De Zárate, A. Gómez-Moratalla, C. Guillem, A. Beltrán, J. Latorre, D. Beltrán, P. Amorós, High-zirconium-content nano-sized bimodal mesoporous silicas, Eur. J. Inorg. Chem. (2006) 2572–2581, https://doi.org/10.1002/ejic.200501140.
[18] A.A. Rownaghi, A. Kant, X. Li, H. Thakkar, A. Hajari, Y. He, P.J. Brennan, H. Hosseini, W.J. Koros, F. Rezaei, Aminosilane-grafted zirconia-titiania-silica nanoparticles/torlon hollow fiber composites for CO_2 capture, ChemSusChem. 9 (2016), https://doi.org/10.1002/cssc.201600082.
[19] T. Ncube, K. Suresh Kumar Reddy, A. Al Shoaibi, C. Srinivasakannan, Benzene, toluene, m-xylene adsorption on silica-based adsorbents, Energy Fuels 31 (2017) 1882–1888, https://doi.org/10.1021/acs.energyfuels.6b03192.
[20] M.A.H. and, J.A. Velasco, M. Asomoza, S. Solís, and F. Rojas, V.H. Lara, Adsorption of Benzene, Toluene, and p-Xylene on Microporous SiO2, (2004). doi:10.1021/IE0204888.
[21] H.O. Seo, D.H. Kim, K.D. Kim, E.J. Park, C.W. Sim, Y.D. Kim, Adsorption and desorption of toluene on nanoporous TiO_2/SiO_2 prepared by atomic layer deposition (ALD): influence of TiO_2 thin film thickness and humidity, Adsorption 19 (2013) 1181–1187, https://doi.org/10.1007/s10450-013-9550-3.
[22] A. Krishnamurthy, H. Thakkar, A.A. Rownaghi, F. Rezaei, Adsorptive removal of formaldehyde from air using mixed-metal oxides, Ind. Eng. Chem. Res. 57 (2018) 12916–12925, https://doi.org/10.1021/acs.iecr.8b02962.
[23] L. Wang, J. Zhang, X. Yi, A. Zheng, F. Deng, C. Chen, Y. Ji, F. Liu, X. Meng, F.-S. Xiao, Mesoporous ZSM-5 zeolite-supported Ru nanoparticles as highly efficient catalysts for upgrading phenolic biomolecules, ACS Catal. 5 (2015) 2727–2734, https://doi.org/10.1021/acscatal.5b00083.
[24] J.H. Smått, S. Schunk, M. Lindén, Versatile double-templating synthesis route to silica monoliths exhibiting a multimodal hierarchical porosity, Chem. Mater. 15 (2003) 2354–2361, https://doi.org/10.1021/cm0213422.
[25] Z.Y. Yuan, B.L. Su, Insights into hierarchically meso-macroporous structured materials, J. Mater. Chem. (2006) 663–677, https://doi.org/10.1039/b512304f.
[26] T. Witoon, S. Bumrungsalee, P. Vathavanichkul, S. Palitsakun, M. Saisriyoot, K. Faungnawakij, Biodiesel production from transesterification of palm oil with methanol over CaO supported on bimodal meso-macroporous silica catalyst, Bioresour. Technol. 156 (2014) 329–334, https://doi.org/10.1016/j.biortech.2014.01.076.
[27] D. Ortiz De Zarate, A. Gomez-Moratalla, C. Guillem, A. Beltran, J. Latorre, D. Beltran, P. Amoros, High-zirconium-content nano-sized bimodal mesoporous silicas, Eur. J. Inorg. Chem. (2006) 2572–2581, https://doi.org/10.1002/ejic.200501140.
[28] C. Sapsanis, H. Omran, V. Chernikova, O.S.- Sensors, undefined 2015, Insights on capacitive interdigitated electrodes coated with MOF thin films: Humidity and VOCs sensing as a case study, Mdpi.Com. (n.d.).
[29] S.D. Hersee, J.M. Ballingall, The operation of metalorganic bubblers at reduced pressure, J. Vac. Sci. Technol. A Vacuum Surf. Film. 8 (1990) 800–804, https://doi.org/10.1116/1.576921.
[30] R.T. Yang, Gas separation by adsorption, Processes (1987).
[31] J.C. Knox, A.D. Ebner, M.D. LeVan, R.F. Coker, J.A. Ritter, Limitations of breakthrough curve analysis in fixed-bed adsorption, Ind. Eng. Chem. Res. 55 (2016)

4734–4748, https://doi.org/10.1021/acs.iecr.6b00516.
[32] T. Sing, K.S.W. Everett, D.H. Haul, R.A.W. Moscou, L. Pierotti, R.A. Rouquerol, J. Siemieniewska, Reporting physisorption data for gas/solid system with special reference to the determination of surface area and porosity, Pure Appl. Chem. 57 (1985) 603–619.
[33] F. Babaie, S.H. Mousavi, A. Mohammad Alizadeh, N. Hazrati, Carbon dioxide capture by modified UVM-7 adsorbent, J. Chem. Pet. Eng. 48 (2014) 91–102, https://doi.org/10.22059/JCHPE.2014.63712.
[34] Z.G. Wu, Y.X. Zhao, D.S. Liu, The synthesis and characterization of mesoporous silica-zirconia aerogels, Microporous Mesoporous Mater. 68 (2004) 127–132, https://doi.org/10.1016/j.micromeso.2003.12.018.
[35] H.L. Tidahy, S. Siffert, J.F. Lamonier, E.A. Zhilinskaya, A. Aboukais, Z.Y. Yuan, A. Vantomme, B.L. Su, X. Canet, G. De Weireld, M. Frere, T.B. N'Guyen, J.M. Giraudon, G. Leclercq, New Pd/hierarchical macro-mesoporous ZrO_2, TiO_2 and ZrO_2-TiO_2 catalysts for VOCs total oxidation, Appl. Catal. A Gen. 310 (2006) 61–69, https://doi.org/10.1016/j.apcata.2006.05.020.
[36] E.J. Park, J.H. Lee, K.D. Kim, D.H. Kim, M.G. Jeong, Y.D. Kim, Toluene oxidation catalyzed by NiO/SiO_2 and NiO/TiO_2/SiO_2: towards development of humidity-resistant catalysts, Catal. Today 260 (2016) 100–106, https://doi.org/10.1016/j.cattod.2015.03.038.
[37] J.E. Szulejko, K.H. Kim, J. Parise, Seeking the most powerful and practical real-world sorbents for gaseous benzene as a representative volatile organic compound based on performance metrics, Sep. Purif. Technol. 212 (2019) 980–985, https://doi.org/10.1016/j.seppur.2018.11.001.
[38] W.W. He, G.S. Yang, Y.J. Tang, S.L. Li, S.R. Zhang, Z.M. Su, Y.Q. Lan, Phenyl groups result in the highest benzene storage and most efficient desulfurization in a series of isostructural metal-organic frameworks, Chem. – A Eur. J. 21 (2015) 9784–9789, https://doi.org/10.1002/chem.201500815.
[39] J. Choma, Ł. Osuchowski, A. Dziura, M. Marszewski, M. Jaroniec, Benzene and methane adsorption on ultrahigh surface area carbons prepared from sulphonated styrene divinylbenzene resin by KOH activation, Adsorpt. Sci. Technol. 33 (2015) 587–594, https://doi.org/10.1260/0263-6174.33.6-8.587.
[40] S. Jafari, F. Ghorbani-Shahna, A. Bahrami, H. Kazemian, Adsorptive removal of toluene and carbon tetrachloride from gas phase using Zeolitic Imidazolate Framework-8: Effects of synthesis method, particle size, and pretreatment of the adsorbent, Microporous Mesoporous Mater. 268 (2018) 58–68, https://doi.org/10.1016/j.micromeso.2018.04.013.
[41] X. Tian, X. Deng, X. Tan, X. Yan, Numerical evaluation of the diffusion enhancement in meso-microporous materials originating from mesopores, Microporous Mesoporous Mater. 245 (2017) 58–63, https://doi.org/10.1016/j.micromeso.2017.02.067.